Sustainable Energy & Fuels

ROYAL SOCIETY OF CHEMISTRY

PAPER

View Article Online
View Journal | View Issue

Check for updates

Cite this: *Sustainable Energy Fuels*, 2022, **6**, 3858

One-step construction of Y, C, and O tridoped g-C₃N₄ as a bifunctional photocatalyst for H₂ evolution and organic pollutant degradation under visible light irradiation†

Ahmed E. Hassan,[abc] Mai S. A. Hussien,[de] Mohamed Hammad Elsayed,[cf] Mohamed Gamal Mohamed,[gh] Shiao-Wei Kuo,[g] Ho-Hsiu Chou,[f] Ibrahim S. Yahia,[ijk] Genxinag Wang*[a] and Zhenhai Wen*[a]

Photocatalytic H₂ production and degradation of pollutants are promising strategies for energy conversion and environmental protection, where highly efficient photocatalysts are required. Herein, a novel type of Y, C, and O tridoped g-C₃N₄ bifunctional photocatalyst was prepared *via* a simple one-step low-cost thermal polymerization technique, which exhibits a significant enhancement in photocatalytic redox efficiency under visible light for H₂ production and degradation of pollutants compared to bulk g-C₃N₄. The optimized Y0.1/C/O tridoped g-C₃N₄ photocatalyst exhibits a remarkable H₂ evolution rate (HER = 2542.4 μmol g⁻¹ h⁻¹) which is 5 times higher than that of pristine g-C₃N₄ with a high apparent quantum yield of 6% at 420 nm, besides excellent degradation efficiencies for organic pollutants (~100, 98.5 and 82.4% for mixed dyes, congo red, and methylene blue, respectively). The influence of Y³⁺ concentration on the photocatalytic performance and electronic structure of Y/C/O−CN was also investigated. The major reactive species involved in the photodegradation process were found to be superoxide (O₂·⁻) radicals. Moreover, the experimental and computational results suggest that the enhanced photocatalytic performance is due to the synergistic effect of Y, C, and O tridoping, which can adjust the band structure of g-C₃N₄, reduce the bandgap, improve visible-light absorption, and accelerate charge separation. This study paves the way to fabricate extremely effective tridoped photocatalysts for efficiently evolving hydrogen under visible light and resolving future environmental pollution.

Received 16th April 2022
Accepted 7th June 2022

DOI: 10.1039/d2se00525e

rsc.li/sustainable-energy

1. Introduction

Energy scarcity and environmental pollution are currently two of the most significant challenges facing human beings; as a result, sustainable social development requires developing green technology.[1] One option is photocatalysis, which is a sustainable and environmentally beneficial process for producing H₂ from H₂O and degrading organic pollutants into harmless end products.[2–6] Photocatalysts are critical for the photoefficiency of these processes. TiO₂ and ZnO have been widely investigated as photocatalytic semiconductors.[7–9] However, the broad bandgap of these conventional photocatalysts (which respond only to UV light) and low light quantum yield restrict their application.

Recent research has focused on g-C₃N₄, a potential metal-free photocatalyst with a high capacity for harvesting visible

[a]CAS Key Laboratory of Design and Assembly of Functional Nanostructures and Fujian Provincial Key Laboratory of Nanomaterials, Fujian Institute of Research on the Structure of Matter, Chinese Academy of Sciences, Fuzhou, Fujian, 350002, China. E-mail: wgx@fjirsm.ac.cn; wen@fjirsm.ac.cn

[b]University of Chinese Academy of Sciences, Beijing, 100049, China

[c]Department of Chemistry, Faculty of Science, Al-Azhar University, Nasr City 11884, Cairo, Egypt

[d]Department of Chemistry, Faculty of Education, Ain Shams University, Roxy, Cairo 11757, Egypt

[e]Nanoscience Laboratory for Environmental and Bio-medical Applications (NLEBA), Department of Physics, Faculty of Education, Ain Shams University, Roxy, Cairo 11757, Egypt

[f]Department of Chemical Engineering, National Tsing Hua University, Hsinchu, 30013, Taiwan

[g]Department of Materials and Optoelectronic Science, Center of Crystal Research, National Sun Yat-Sen University, Kaohsiung 80424, Taiwan

[h]Chemistry Department, Faculty of Science, Assiut University, Assiut 71516, Egypt

[i]Research Center for Advanced Materials Science (RCAMS), King Khalid University, Abha 61413, P. O. Box 9004, Saudi Arabia

[j]Advanced Functional Materials & Optoelectronic Laboratory (AFMOL), Department of Physics, Faculty of Science, King Khalid University, 9004, Abha, Saudi Arabia

[k]Semiconductor Lab., Department of Physics, Faculty of Education, Ain Shams University, Roxy, 11757 Cairo, Egypt

† Electronic supplementary information (ESI) available. See https://doi.org/10.1039/d2se00525e

3858 | *Sustainable Energy Fuels*, 2022, **6**, 3858–3871

This journal is © The Royal Society of Chemistry 2022

Published on 07 June 2022. Downloaded by National Sun Yat Sen University on 11/15/2022 10:22:28 AM.

light with a small bandgap (∼2.7 eV) besides appropriate conduction and valence band positions.[10–13] Additionally, g-C_3N_4 has the following advantages: a simple synthesis, non-toxicity, and low cost with earth-abundant C and N, in addition to stability under both temperature and chemical conditions. Thus, g-C_3N_4 offers a wide variety of applications in organic pollutant degradation and H_2 generation under visible light[14–16] and other fields.[17–20] Although g-C_3N_4 exhibits favorable photocatalytic properties, many drawbacks remain, including a high recombination rate of photogenerated electron–hole pairs, poor efficiency of using visible light, and small surface area.[21,22]

Various approaches for addressing these issues have been developed, including metal and nonmetal doping,[23–25] deposition with noble or transition metals,[26,27] the introduction of vacancy defects,[28] copolymerization,[29] coupling with other semiconductors,[30] and construction of various nano-architectures.[31,32] Among the various strategies, doping is one of the most efficient and suitable techniques available. Metal doping, particularly with rare-earth elements, is a well-studied approach. High photocatalytic activity has been reported for newly synthesized Y-doped semiconductors such as Y-doped g-C_3N_4, Y-TiO_2, and Y-SnO_2 with small band gaps.[33–35] It has been suggested previously that large radius rare-earth ions exceed the majority of other metals and nonmetals in enhancing the photogenerated electron–hole separation in the photocatalytic process. Besides, nonmetal doped g-C_3N_4 can also absorb visible light; carbon or oxygen doping has recently demonstrated promising photo-response and catalytic efficiency as a result of the fast separation of photogenerated e^- and h^+, leading to improved photocatalytic and visible light utilization.[36–38] Moreover, codoping g-C_3N_4 with two different types of atoms, such as C, O codoping,[39–41] P, C codoping,[42] and P, O codoping,[43] results in higher photocatalytic activity and unusual physicochemical properties compared to single element doping. Wu *et al.* synthesized C/O codoped g-C_3N_4 using glutathione as a source of O and C, in which the H_2 evolution activity was about 80 times greater than that of g-C_3N_4.[40] Recently, Jing *et al.* developed a one-step polymerization technique for toluene oxidation and bisphenol A photodegradation using carbon and oxygen codoped g-C_3N_4.[39] In addition, the benefits of metal and nonmetal dopants can be combined by codoping or tridoping, resulting in enhanced photocatalytic activity.[44] As far as we know, the synergistic effect of metal (Y) and nonmetal (C and O) doping on the g-C_3N_4 photocatalyst for H_2 production and pollutant degradation has not been reported yet.

In the present work, a series of Yx, C, O tridoped g-C_3N_4 (x is the amount of Y salt, x = 0.01, 0.1, 0.25, 0.5, and 1 g) photocatalysts are successfully synthesized using a one-step low-cost thermal polymerization method to precisely control the bandgap of organic photocatalysts, which resulted in bandgap alterations between 2.75 and 1.90 eV by introducing malonic acid and varying the yttrium amounts. Furthermore, using this approach, the band positions and photocatalytic performance of polymer semiconductors are correlated. To demonstrate the morphology, structure, and composition of the improved materials we fabricated, we performed a series of

characterization experiments. In addition, the physicochemical properties of Yx, C, O tridoped g-C_3N_4, as well as the suggested mechanism for enhancing the photocatalytic activity of these photocatalysts, have been thoroughly investigated. Moreover, as a bifunctional photocatalyst, it demonstrates excellent photocatalytic activity and stability under visible-light irradiation for both H_2 production and degradation of pollutants including congo red (CR), methylene blue (MB), and a mixture of these two dyes. The effect of yttrium ion (Y^{3+}) concentration on the Y/C/O–CN electronic structure and photocatalytic performance is discussed in detail. Combining experimental and computational methods, the critical effect of the g-C_3N_4 tridoping with Y, C, and O atoms on the photocatalytic activity has been explored in detail.

2. Experimental procedure

2.1 Preparation of photocatalysts

The Y, C, and O tridoped g-C_3N_4 photocatalysts were synthesized as follows. First, 10 g of urea, 0.5 g of malonic acid, and various quantities of yttrium nitrate (0.01, 0.1, 0.25, 0.5, and 1 g) were mixed and ground in a mortar. Then, the powders were transferred to a ceramic crucible with a cover and then annealed in a muffle furnace for 2 h at 550 °C (heating rate 5 °C min^{-1}). Finally, after cooling to ambient temperature and grinding them into fine powders, the Yx, C, O tridoped g-C_3N_4 samples were obtained and denoted with respect to yttrium as Yx/C/O–CN (x = 0.01, 0.1, 0.25, 0.5, and 1 g), respectively. To provide a point of comparison, C and O codoped g-C_3N_4 (C/O–CN) was prepared using the same procedure without adding yttrium nitrate with reference to a method reported previously.[39] In contrast, pure g-C_3N_4 (CN) was prepared directly by calcination of urea under the same conditions. The Y, C, and O tridoped g-C_3N_4 photocatalysts were synthesized according to the procedure shown in Fig. 1.

2.2 Characterization

Powder X-ray diffraction (PXRD) was performed using an X'Pert Pro diffractometer with Cu Kα radiation. A Bruker Tensor-27 FTIR spectrophotometer was used to collect the infrared (IR) spectra with a resolution of 4 cm^{-1}. X-ray photoelectron spectroscopy (XPS) spectra were collected using an ULVAC-PHI PHI 5000 Versaprobe II chemical analysis electron spectrometer (ESCA). The ^{13}C nuclear magnetic resonance (^{13}C NMR) spectra were measured using a Bruker Avance 500 solid-state NMR spectrometer. The sample morphology was examined using a scanning electron microscope (SEM, JEOL JSM-6500). Transmission electron microscopy (TEM) images were recorded using a JEOL 2100 instrument that was operated at an accelerating voltage of 200 kV. A Hitachi U-3300 spectrophotometer was used to record UV-vis diffuse reflectance spectra (UV-vis DRS). HOMO energy levels were determined with the help of an ultraviolet photoelectron spectrometer (model AC-2). When the bandgap (E_g) was subtracted from the HOMO energy levels, it was possible to calculate the LUMO energy levels. A Hitachi F-7000 fluorescence spectrophotometer (λ_{ex} = 370 nm) was used to
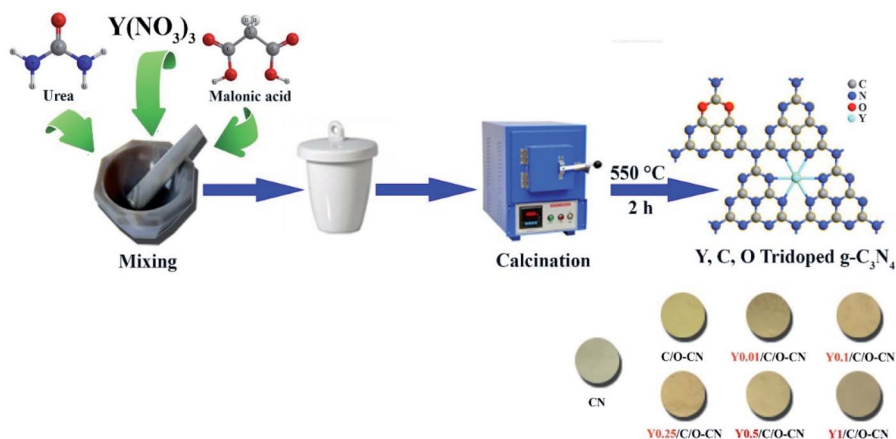
Fig. 1 Schematic illustration of the synthesis of Yx/C/O tridoped CN samples.

capture the photoluminescence (PL) spectra. Thermal gravimetric analysis (TGA) was performed under N_2 using a TGA Q-50 analyzer with temperature ranging from 40 to 800 °C at a heating rate of 20 °C min^{-1}. The specific surface area was determined using the Brunauer–Emmett–Teller (BET) technique on a Micromeritics ASAP 2020 at 77 K by analyzing N_2 adsorption–desorption isotherms.

2.3 Photocatalytic hydrogen production

H_2 production experimental studies were carried out at room temperature. In this reaction, 1.5 mg of the photocatalyst powder was dispersed in an aqueous solution, including a co-catalyst of Pt (5 wt%) and triethanolamine (TEOA; 10 vol%) as a sacrificial agent. Before light irradiation, Ar bubbling was used for degassing the resultant mixture after ultrasonically processing extensively. The suspension was exposed to 1000 W m^{-2} (1 sun) solar simulator radiation at $\lambda > 420$ nm. In this study, a Shimadzu gas chromatograph (GC-2014 with a thermal conductivity detector) was used to measure the quantity of H_2 evolved while argon served as the carrier gas. Apparent quantum yields (AQY) for Y0.1/C/O–C_3N_4 hydrogen production were estimated as follow:

$$AQY = \frac{2 \times \text{number of evolved } H_2 \text{ molecules}}{\text{number of incident photons}} \times 100\%$$

2.4 Photocatalytic degradation of organic pollutants

As a way to check the synthetic materials' photocatalytic efficiency, several dye solutions were photodegraded under visible light. Two different dye solutions (CR & MB) were photodegraded firstly, followed by combining the two dye solutions. First, 5 mg of catalyst was dissolved in 25 mL of CR (50 ppm) or MB (10 ppm) aqueous solution. Then, the suspension solution was stirred for 30 minutes in the dark to achieve adsorption–desorption equilibrium. A UV-vis spectrophotometer was used to monitor the dye concentration, and the λ_{max} peak intensity decreased as the reaction time progressed (CR and MB have λ_{max} values of 500 and 664 nm, respectively). The photocatalytic

reaction of these model dye solutions was studied in detail to find the best Y/C/O tridoped g-C_3N_4 photocatalyst composition. Using the optimized catalyst, a mixture of CR (25 ppm) and MB (10 ppm) solutions was tested for photodegradation. Additionally, the stability of the materials was investigated using five cycle experiments.

2.5 Photoelectrochemical measurements

On a Zahner Zennium E workstation, the photoelectrochemical experiments were performed with a three-electrode cell. An Ag/AgCl electrode, Pt wire, and FTO glass were employed as the reference electrode, counter electrode, and working electrode, respectively. Around 5 mg photocatalyst was dispersed in a methanol solution (1 mL) containing 30 mL Nafion and sonicated for 30 minutes. This was followed by drop-casting of 200 mL of the above solution on the FTO glass. As an electrolyte, 0.5 M Na_2SO_4 aqueous solution was prepared in this experiment. Under LED light irradiation, the photo and dark currents were recorded using a 1.0 V constant potential and a 20 second light on/off period following a predetermined time interval.

2.6 Computational details

The density functional theory (DFT) method implemented in the Materials Studio CASTEP code[45] was used for all calculations. Using the GGA-PBE functional,[46,47] the geometrical structure of the presented models can be optimized besides calculating their optical and electronic properties. For simulation, the system's energy was converged to 10^{-5} eV, and the maximum force between atoms and the maximum displacement were 3×10^{-2} eV Å^{-1} and 1×10^{-3} Å, respectively. The Grimme technique for DFT-D correction was used to characterize van der Waals interactions. The $2 \times 2 \times 1$ supercells are duplicated on the x–y plane. In contrast, the vacuum space along the z-direction has been set to 20 Å to prevent periodic structures from interacting with each other. The plane-wave basis set has a 500 eV cutoff energy. For the structural optimizations, the Brillouin zone was described by Monkhorst–Pack ($3 \times 3 \times 1$) K-points. The supercell's high-quality band structure

(BS), the density of states (DOS), and optical properties are achieved by using denser K-points of $5 \times 5 \times 1$.

3. Results and discussion

3.1 Characterization

In this study, the crystal structures of pristine CN and Yx/C/O–CN (x = 0.01, 0.1, 0.25, 0.5, and 1 g) were investigated using PXRD (Fig. 2a). The strong diffraction peak observed at 27.4° corresponds to the (002) plane of the interlayer stacking reflection of the conjugated aromatic system. In comparison, the other weak peak (100) centered at 13.5° was related to the tri-s-triazine unit's in-plane structure repeating pattern (JCPDS no. 87-1526).[48] The XRD patterns of Yx/C/O–CN are similar to those of pristine CN, indicating that the tridoped Y, C, and O did not have an obvious effect on the pristine CN crystal structure. The doped samples had no obvious Y or yttrium oxide diffraction peaks, showing that Y was widely spread across the g-C$_3$N$_4$ matrix and incorporated into in-planes as well as coordinated via Y–N bonds to the g-C$_3$N$_4$ matrix[35] without other impurity phases.

Fig. 2a shows that the two diffraction peaks become weaker with a rising Y ratio for Yx/C/O–CN samples owing to the decreased crystallinity and the defects caused by incomplete polymerization after heteroatom doping[33,35] (Table S1†). This might be because the incorporation of Y^{3+} ions into g-C$_3$N$_4$ in addition to replacing N atoms with C or O atoms shortens the bond length and reduces the size of the polymer.[39,49] The slight shift to the lower angle of the (002) peak as the yttrium ratio increases (Fig. 2a) can be attributed to the increased interlayer distance caused by Y-doping and partial replacement of N atoms with C or O atoms.[41] The change in peak location corresponds to the change in the yttrium equivalent. According to the Scherrer equation, raising Y doping to 1 g significantly reduces the average crystallite size of the photocatalyst from 2.569 nm to 1.557 nm. In contrast to pure CN, the doped samples had more lattice strain, which reduces the material's crystallinity (Table S1†).

Fig. 2b shows the FT-IR spectra of the synthesized photocatalysts (CN, C/O–CN, and Yx/C/O–CN). The FT-IR spectra of Yx/C/O–CN catalysts are nearly identical to pure g-C$_3$N$_4$, with broad peaks corresponding to the stretching vibration of N–H bonds at ~3000–3500 cm^{-1},[49] which is equivalent to uncondensed NH$_2$ groups. The ring breathing vibration of tri-s-triazine units is responsible for the sharp peak at around 810 cm^{-1}.[40] Several strong peaks between 1249 and 1638 cm^{-1} correspond to C=N and C–N ring stretches.[39] It should be noted that when compared to the pure CN, these peak values (CN
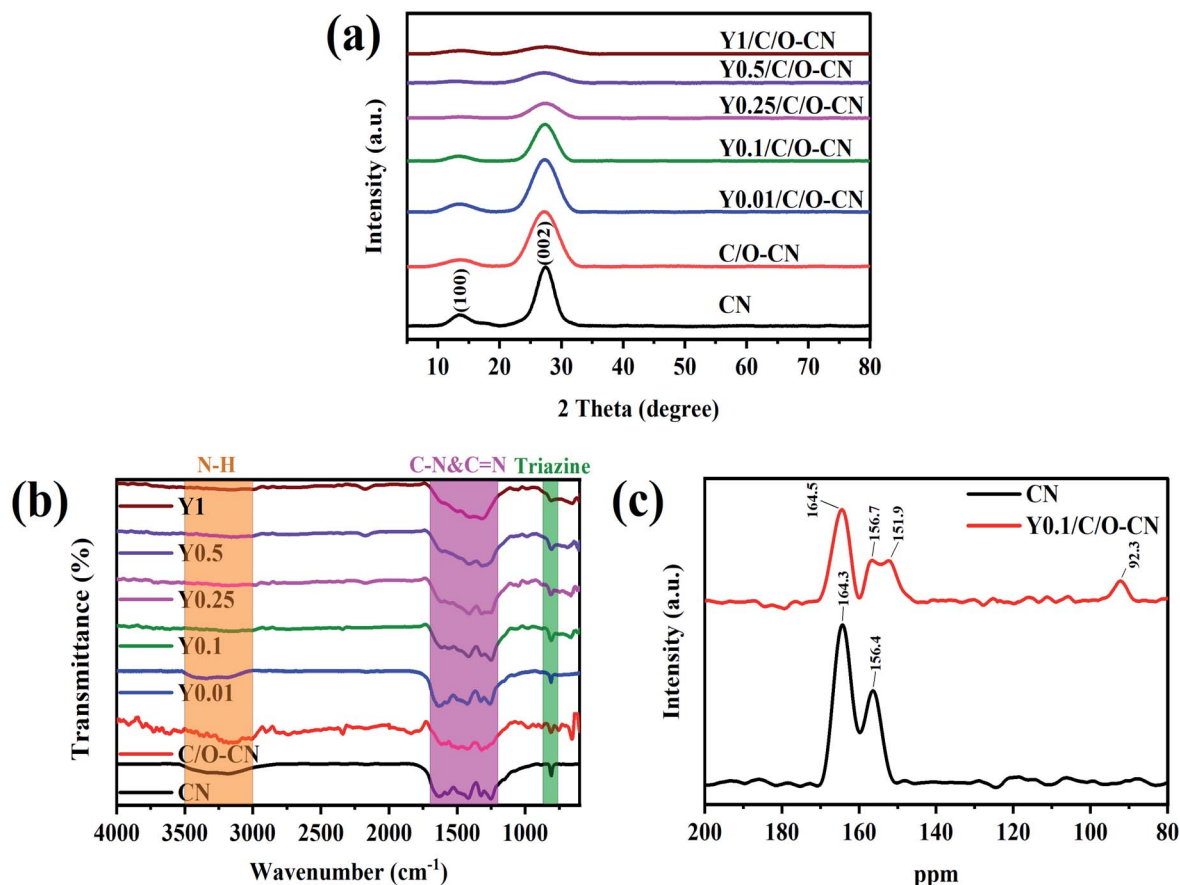

Fig. 2 (a) XRD patterns and (b) FT-IR spectra of bulk-CN, C/O–CN, and Yx/C/O tridoped CN samples, and (c) solid-state ^{13}C NMR spectra of bulk-CN and Y0.1/C/O–CN samples.

heterocycles) move slightly higher in frequency with a drastically decreased intensity in the doping system (Fig. S1†), owing to the Y, C, and O doping, as well as the higher electronegativity of O atoms, suggesting that this portion of C–N became C–O, as the C–O bond appears at higher frequencies due to the higher electronegativity of O atoms.[38] Moreover, the tridoped system exhibits a new absorption peak at 2100–2200 cm^{-1} assigned to the C≡N stretching vibration[50] (Fig. 2b). In conclusion, adding Y, C, and O atoms into pure g-C$_3$N$_4$ does not affect the skeleton structure, consistent with XRD results.

The chemical state of C atoms and structural changes were studied in detail using the ^{13}C solid-state NMR technique (Fig. 2c). The NMR spectrum of g-C$_3$N$_4$ (CN) exhibits two signals at 164.3 and 156.4 ppm, which are assigned to the terminal CN$_2$–NH$_x$ and CN$_3$ chemical shifts, respectively.[39,40] The Y0.1/C/O–CN signals exhibit a slightly higher chemical shift in comparison to bulk CN besides new signals at 92.3 (O–C–O; 90–100 ppm)[11,39] and 151.9 ppm;[38,40] this indicates the formation of a new state of carbon due to the incorporation of oxygen and carbon atoms, as well as indicating that malonic acid has been conjugated to the g-C$_3$N$_4$ matrix and the structure of g-C$_3$N$_4$ remained unchanged. The observed left-shifted peaks with weakening signals in the Y0.1/C/O–CN sample could result from introducing oxygen lone-pairs and increasing the electron density around carbon atoms.[38]

By TGA, it is possible to determine the thermal stability of pure CN and doped systems (Yx/C/O–CN) over a temperature range of 40–800 °C (Fig. S2†). The TGA curve of pure CN is relatively stable at temperatures below 500 °C, and 100% decomposition is achieved above 710 °C.[51] The high temperatures destroy the chemical bonding between the triazine rings in g-C$_3$N$_4$, producing nitrogen and cyano fragments.[11] The amount of undecomposed sample in Y/C/O g-C$_3$N$_4$ photocatalysts was determined to be 0.12, 1.97, 17.01, 27.94, and 40.70% for Y0.01/C/O–CN, Y0.1/C/O–CN, Y0.25/C/O–CN, Y0.5/C/O–CN, and Y1/C/O–CN, respectively. This residual solid represents the amount of Y in the photocatalysts. Due to codoping, the thermal stability of g-C$_3$N$_4$ decreases significantly as the yttrium content increases.[52]

The surface elemental and chemical bonding states of pure g-C$_3$N$_4$ (CN), C/O–CN, and Yx/C/O–CN were all determined by XPS analysis. There are three distinct peaks in the survey spectra of all samples (Fig. 3a) at around 288 eV (C 1s), 398 eV (N 1s), and 532 eV (O 1s).[40] Additionally, only Yx/C/O–CN samples showed a weak Y 3d peak at about 158 eV.[33] Deconvolution of XPS spectra of all elements in CN, C/O–CN, and Y0.1/C/O–CN samples was plotted in Fig. 3b–e. The high-resolution C 1s spectra show three peaks at 284.4, 285.7, and 287.8 eV, corresponding to the C–C bond, C–O bond, and the C atoms connected to N atoms within the aromatic ring of N═C–(N)$_2$, respectively.[39,41] All the peaks in the Y0.1/C/O–CN sample appear slightly displaced, suggesting that a specific reaction happened due to the malonic acid introduction, which dramatically changed the C-atom chemical environment. The C/N atomic ratio (Table S2†) for C/O–CN and Yx/C/O–CN samples is 0.84–1.21, higher than that for pure CN (0.82). Meanwhile, the N═C–(N)$_2$: C–C area ratio for Y0.1/C/O–CN is 6.71, which is lower

than those of C/O–CN and pure-CN (7.08 and 8.65, respectively) (see Table S3†). It is believed that the replacement of small amounts of N by C and O atoms has increased the atomic ratio of C/N as well as causing a decrease in the value of N═C–(N)$_2$: C–C.[36,40] There is also an increase in the C–O and C–C peak intensity for Y0.1/C/O–CN (Fig. 3b and Table S3†), indicating an increased number of C–O and C–C groups.[40] The N 1s high-resolution spectra in Fig. 3c are deconvoluted into three peaks located at 400.7, 399.2, and 398.2 eV, which are assigned to the terminal amino functional groups (C–NH$_x$), the inner tertiary nitrogen (N-(C)$_3$) groups, and the sp^2-hybridized nitrogen (C═N–C) in triazine rings, respectively.[39,40] When malonic acid is introduced into the polymerization process of carbon nitride, the two peaks at 398.2 and 399.2 eV in the Y0.1/C/O–CN spectrum appear to shift. The introduction of tri-doping atoms significantly affected the chemical environment of N. In the presence of C and O doping, the area ratio of C═N–C decreased from pure-CN (59.59) to Y0.1/C/O–CN (48.88) (see Table S4†). This supports the substitution of C or O atoms for the sp^2 N-atom in triazine rings.[36,38,40] For pure g-C$_3$N$_4$, the O 1s XPS spectrum exhibits peaks at 531.9 and 533.6 eV (Fig. 3d), corresponding to adsorbed H$_2$O and O$_2$ molecules on the specimen holder, respectively.[40] In contrast, the signal at 530.4 eV indicates the existence of C–O groups.[40] The corresponding peak position in the Y0.1/C/O–CN and C/O–CN samples will have a particular offset. The higher intensity of the C–O species peak proves the presence of more C–O species in both Y0.1/C/O–CN and C/O–CN samples (Fig. 3d and Table S5†). The binding energies of Y 3d spin–orbit split peaks (3d$_{5/2}$ and 3d$_{3/2}$) have broad peaks between 154 and 164 eV (ref. 33 and 35) (Fig. 3e), which confirmed the existence of Y^{3+} ions in Y0.1/C/O–CN samples. The Y concentrations determined from XPS data were 0.08, 0.64, 1.78, 3.02, and 5.53 atomic% for Y0.01/C/O–CN, Y0.1/C/O–CN, Y0.25/C/O–CN, Y0.5/C/O–CN, and Y1/C/O–CN, respectively (Table S2†).

The morphologies of CN and Yx/C/O–CN samples were investigated using SEM images. As illustrated in Fig. S3a† and 4a, pure CN exhibits a compact *Tremella*-like structure, whereas Yx/C/O–CN exhibits a curled sheet structure. The nanosheets are curled to reduce the surface tension.[51] When the yttrium content is increased to 0.1 g, the sample exhibits more and smaller tubular structures (Fig. 4a), in which photogenerated charge carriers may be separated and migrate to the surface of the material more easily. This matches the less crystallized structure deduced from XRD patterns.[53] However, when the yttrium content was increased to 1 g (Y1/C/O–CN), the sample exhibited an obvious irregular blocky structure (Fig. S3a†). The above results indicate that adding yttrium and malonic acid promotes the transition of a layered stacking structure to a tubular-like structure.

TEM images of pure CN and Yx/C/O–CN samples (Fig. S3b† and 4b) exhibit a sheet-like structure with apparent pores, and Y, C, and O doping reduces the sheet size in all samples.[35] No doping-related particles were found in the Yx/C/O–CN samples, confirming that the Y, C, and O species were doped into the g-C$_3$N$_4$ lattices, in accordance with the XRD data. Clearly, there is no remarkable difference between CN, Y0.01/C/O–CN, Y0.1/C/
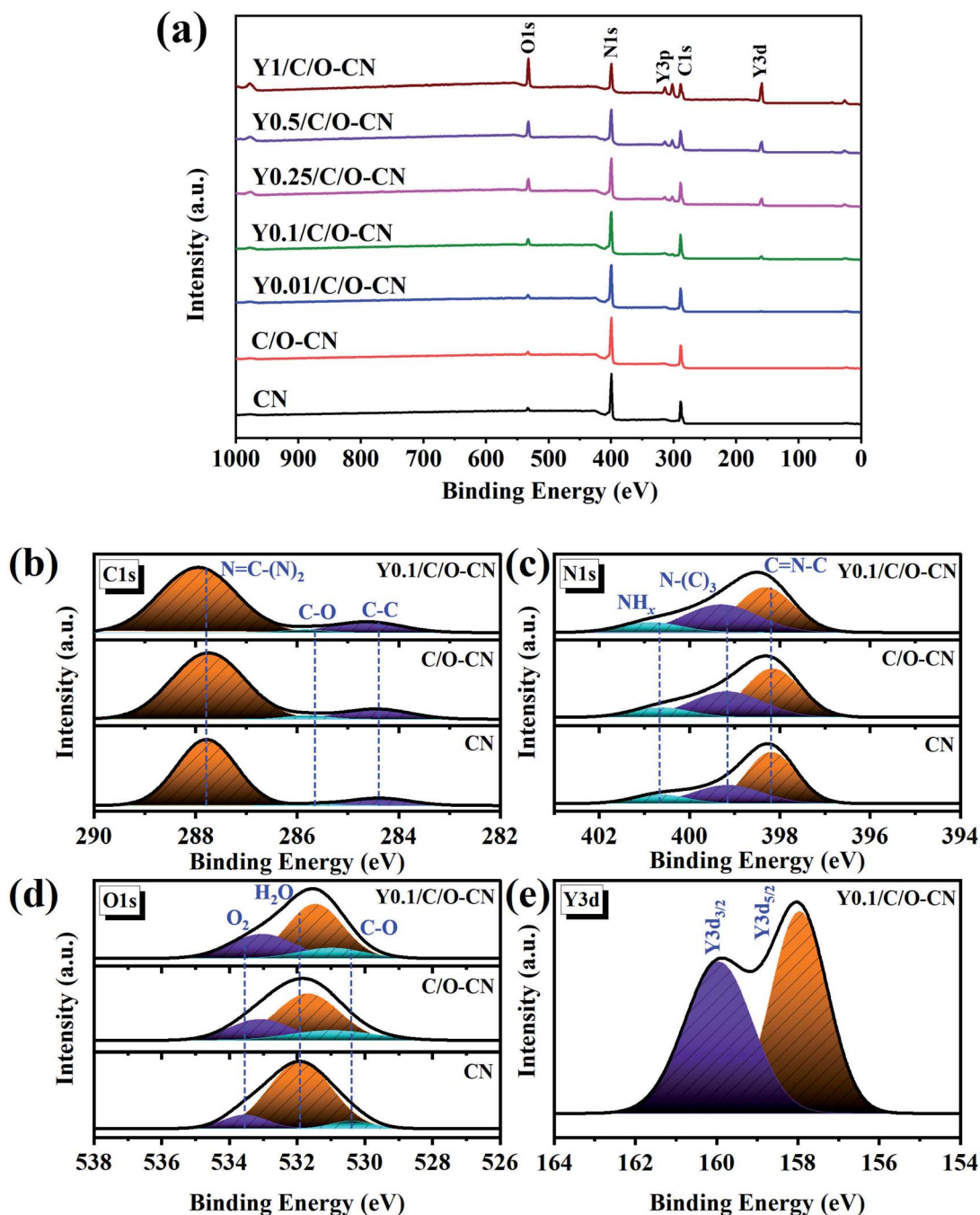
Fig. 3 (a) XPS survey spectra of bulk-CN, C/O−CN, and Yx/C/O tridoped CN samples; (b) C 1s, (c) O 1s, (c) N 1s, and (d) Y 3d high-resolution spectra of Y0.1/C/O−CN.

O−CN, and Y0.25/C/O−CN samples. However, when the yttrium content increased to 0.1 g, the TEM image of Y0.1/C/O−CN was nearly transparent (Fig. 4b), indicating the formation of an ultrathin nanosheet with curled edges. Meanwhile, the further increase in the Y doping ratio over 0.25 resulted in a thick and interlayer-like structure without noticeable pores due to the large aggregates of Y atoms that are irregularly stacked together (Fig. S3b†).

There are more active sites and enhanced light absorption in the two-dimensional layered structure, which promotes photocatalytic activity improvement. The results shown above are similar to those obtained from SEM and the specific surface area. It has been demonstrated that adding yttrium and malonic acid can increase the number of active sites and alter the morphology. Furthermore, the corresponding energy dispersive spectrum (EDS) of the prepared Y0.1/C/O−CN photocatalyst confirmed the presence of C, N, O, and Y elements (Fig. 4c).

Fig. 4d and e show the BET specific surface areas and Barrett–Joyner–Halenda (BJH) pore size distribution curves of CN,
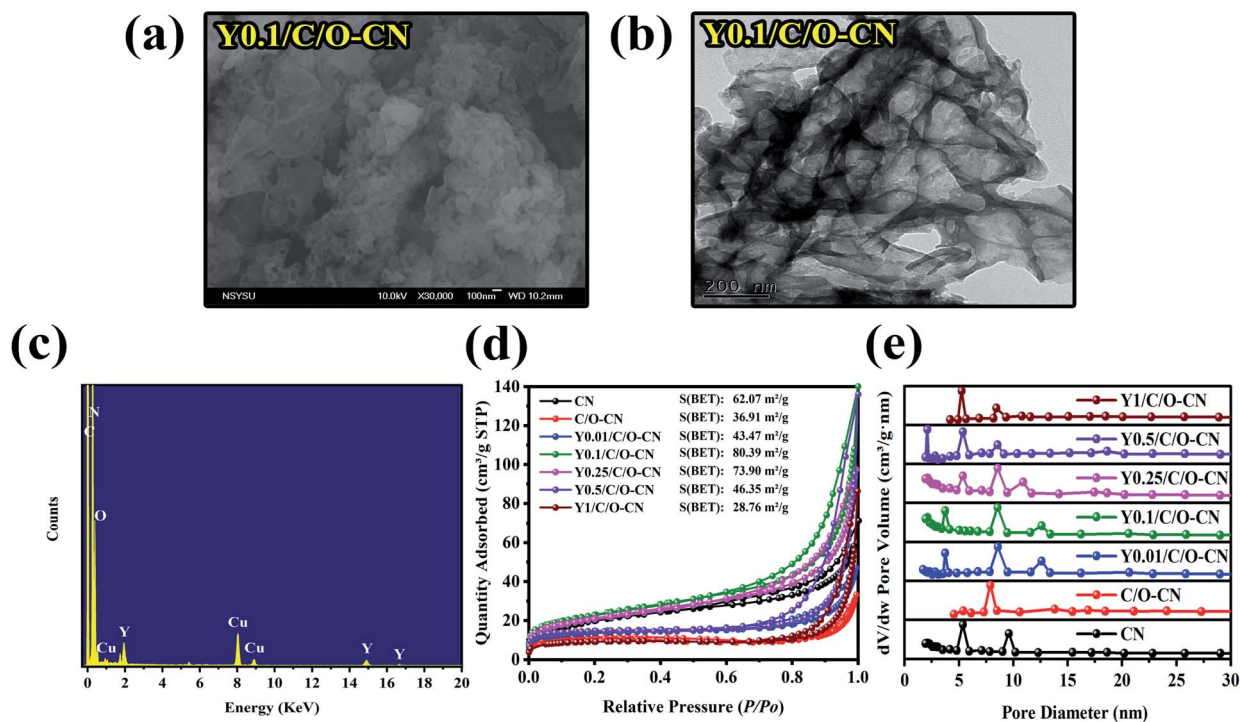
Fig. 4 (a) SEM images and (b) TEM images of the Y0.1/C/O tridoped CN sample. (c) EDS spectra of the Y0.1/C/O−CN sample. (d) N₂ sorption isotherms at 77 K and (e) pore size distribution profiles of bulk-CN, C/O−CN, and Y*x*/C/O tridoped CN samples.

C/O–CN, and Y*x*/C/O–CN photocatalysts. Across all samples, type IV isotherms with H₃ hysteresis loops were observed.[54] The isotherms demonstrate a high uptake of N₂ due to capillary condensation, which indicates the characteristic of mesoporous materials.[55] Hysteresis loops of type H₃ are frequently observed at ∼0.6 < P/P_0 < 1 in all isotherms on non-rigid aggregates of plate-like particles. Furthermore, Y/C/O–CN has a better N₂ adsorption capability than pure CN, implying that Y, C, and O elements in CN are advantageous for mesopore formation. Y0.1/C/O–CN had a much larger specific surface area (S_{BET}) (80.39 m² g⁻¹) than C/O–CN (36.91 m² g⁻¹) or pure CN (62.07 m² g⁻¹) (see Fig. 4d). The S_{BET} of C/O–CN exhibits a remarkable decrease relative to bulk-CN because of partial pore blockages and framework defects due to C and O doping.[56] Nevertheless, the proper addition of Y can increase the BET surface area due to the large radius of Y, which increases the interlayer distance and inhibits the crystal growth of graphitic carbon nitride (Table S1†), leading to the formation of more secondary particles[44,57] and hence more active sites, but when the doping ratio is too large the molecules aggregate and block the active sites. The higher specific surface area is expected to increase the number of active sites that may be exposed to photocatalytic degradation and H₂ evolution. A good agreement exists between the specific surface area of photocatalysts and their morphology-defined structure. Additionally, the pore size distribution curves indicate that the Y*x*/C/O–CN are rich in pores with diameters ranging from 1 to 20 nm (Fig. 4e), indicating that the mesoporous structure of tridoped CN was well-developed. Interestingly, the C/O–CN sample has a pore size distribution centered at 8 nm, representing one kind of pore

structure in the sample. In addition, it has a smaller total pore volume (0.034 cm³ g⁻¹) compared with other samples (Table S6†), which agrees well with the dramatic decrease in the BET result. On the other hand, the total pore volume of the Y0.1/C/O–CN photocatalyst is much larger than that of the bulk CN, which facilitates mass transfer. Such increased BET surface area and pore volume of Y.01/C/O–CN are expected to provide more exposed active sites for reactants, which should be more favorable for the photocatalytic reaction. Table S6† summarizes the textural properties. As the doping ratio of Y increases, both the BET surface area and pore volume increase until the doping ratio reaches 0.25.

3.2 Optical and photoelectrochemical properties

The diffuse reflectance spectra (DRS) of all samples are shown in Fig. 5a. CN exhibits an absorption edge at ∼450 nm, while the Y*x*/C/O–CN samples shifted to a longer wavelength, which intensified as the Y doping ratio decreased. The redshift of the adsorption edge in Y*x*/C/O–CN photocatalysts results from charge transfer between Y³⁺ d-electrons and g-C₃N₄ conduction/valence bands.[35] Thus, doping with Y, C, or O enhances light absorption and forms more ($e^−$)–(h^+) pairs, resulting in increased photocatalytic efficiency. The optical bandgaps (E_g) (Fig. 5b) were determined using the Kubelka–Munk (KM) method, which is illustrated in the following equation:

$$(F(R_\infty)h\nu)^2 = A(h\nu - E_g)$$

where $F(R_\infty)$, h, ν, A, and E_g are the Kubelka–Munk function, Planck constant, light frequency, a constant, and bandgap
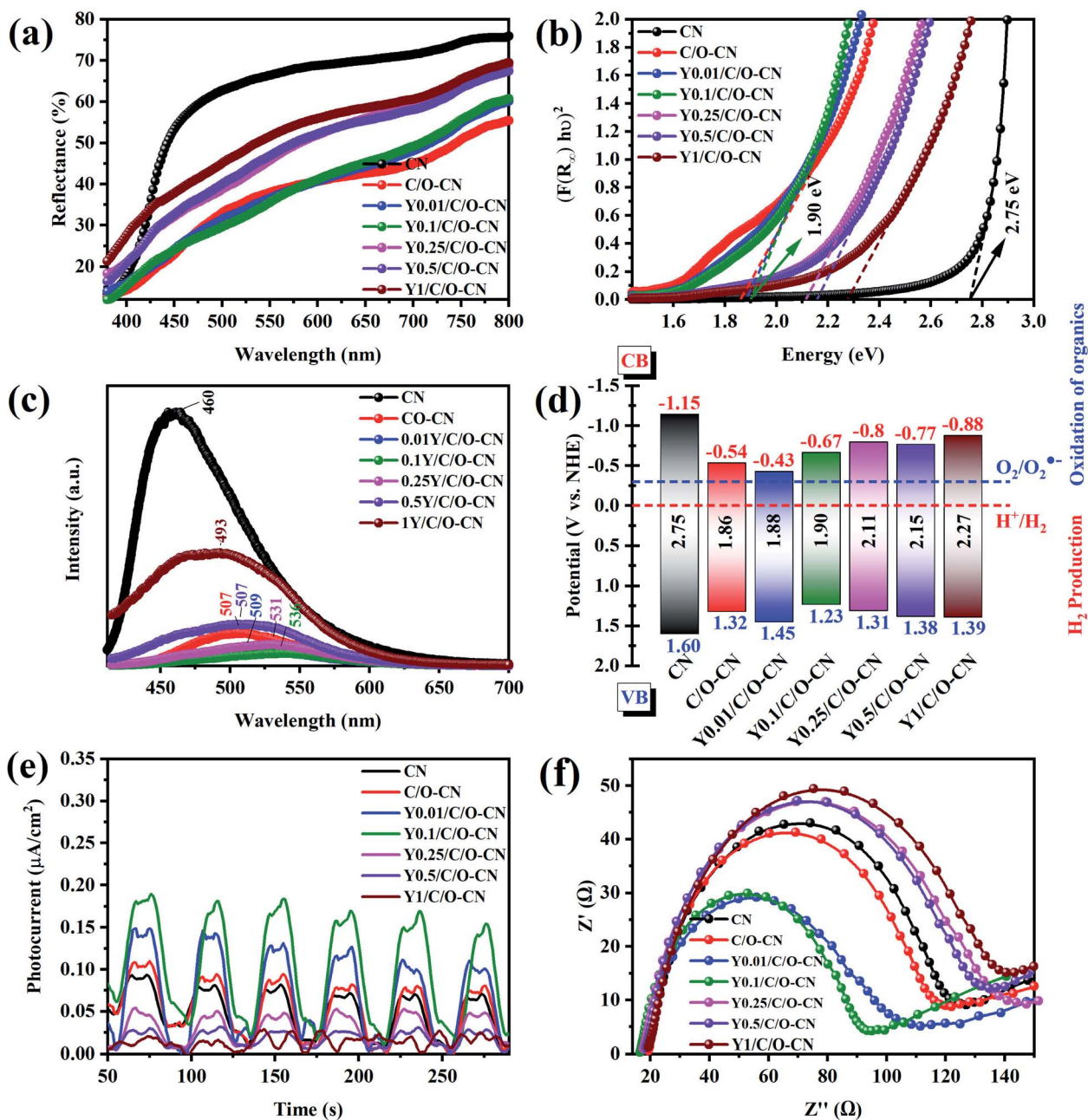
Fig. 5 (a) UV-vis DRS, (b) schematic illustration of the calculated bandgaps energy, (c) PL spectra, (d) band structure diagram, (e) photocurrent responses, and (f) EIS of bulk CN, C/O−CN, and Yx/C/O tridoped CN samples.

energy, respectively. The corresponding band gap values of pure CN, C/O–CN, Y0.01/C/O–CN, Y0.1/C/O–CN, Y0.25/C/O–CN, Y0.5/C/O–CN, and Y1/C/O–CN are 2.75, 1.86, 1.88, 1.90, 2.11, 2.15, and 2.27 eV, respectively (Fig. 5b and Table S6†). The variation of the bandgap value between 2.75 eV (g-C$_3$N$_4$) and 1.88 eV (Y0.01/C/O–CN) is clearly due to the codoping of C and O, as well as increasing the yttrium content in the photocatalysts.[35,39] A further increase in the amount of yttrium (Y1/C/O–CN) results in a broader bandgap (2.27 eV). Consequently, the addition of a suitable doping ratio (Y0.1/C/O–CN) changed the optical properties and light-harvesting capabilities of g-C$_3$N$_4$. This

finding suggests that by varying the amount of Y in the photocatalyst, the E_g values can be modulated.

UPS measurements indicate that the valence band (VB) edges of pure CN, C/O–CN, Y0.01/C/O–CN, Y0.1/C/O–CN, Y0.25/C/O–CN, Y0.5/C/O–CN, and Y1/C/O–CN are calculated to be 1.60, 1.32, 1.45, 1.23, 1.31, 1.38, and 1.39 eV, respectively (Fig. 5d), according to the reference standard for which 0 V *vs.* the normal hydrogen electrode (NHE) equals −4.44 eV *vs.* vacuum. All energy levels were converted from the absolute energy levels calculated by UPS (Fig. S3†) to values relative to NHE. Meanwhile, when the E_g is subtracted from the VB energy levels, it is possible to calculate the

conduction band (CB) edge positions. The calculated CB potentials for pure CN, C/O–CN, Y0.01/C/O–CN, Y0.1/C/O–CN, Y0.25/C/O–CN, Y0.5/C/O–CN, and Y1/C/O–CN were −1.15, −0.54, −0.43, −0.67, −0.80, −0.77, and −0.88 eV, respectively. Using CB energy levels as a guide, all samples should undergo a photocatalytic reduction of protons to H_2. The schematic diagram in Fig. 5d illustrates the band structure of all photocatalysts as well as the reduction levels for H^+/H_2 and $O_2/O_2^{\cdot-}$.

PL, photocurrent, and EIS measurements were conducted to reveal the promoted separation efficiency and transfer of photoinduced charge carriers.[58–62] The photoluminescence emission spectra of CN had a strong emission maximum at 460 nm attributed to emissions of band edges containing π-conjugated states, showing fast recombination of photoexcited carriers (Fig. 5c). On the other hand, the Yx/C/O–CN samples show a much weaker intensity and shift to longer wavelengths (centered at 493–536 nm) due to the n → π* transition.[63] This indicates that adding an O atom can significantly accelerate the excited electron transfer while also preventing electron–hole recombination. The signal redshift is most likely caused by the narrowing of Yx/C/O–CN bandgaps.[64] Y0.1/C/O–CN had the lowest emission intensity, indicating that there was less photogenerated charge recombination and extensive light harvestability due to narrowband states, enhancing photocatalytic activity[65] and correlating with the photocatalytic H_2 evolution performance. It was concluded from these findings that the addition of Y, C, and O doping could improve the photogenerated carrier separation efficiency.

The photocurrents for all samples are shown in Fig. 5e to further evaluate their electrochemical properties and photogenerated charge separation capability. The results showed that Y0.1/C/O–CN has the highest photocurrent density of all the samples, consistent with its photocatalytic activity, which can be attributed to the effectively prevented recombination of charge and the promoted drastic separation of photogenerated electrons.[40] Furthermore, after six cycles of on/off lighting with a 25 second interval, all samples showed consistently positive photocurrent responses, suggesting high photoelectrochemical stability of all samples.

The electrochemical impedance spectra (EIS) of the bulk-CN, C/O–CN, and Yx/C/O–CN (Fig. 5f) showed that the Y0.1/C/O–CN sample possessed the smallest semicircle diameter among these prepared samples, suggesting a considerable improvement in electrical conductivity and efficient separation of electron–hole pairs over Y0.1/C/O–CN.[41] PL and photocurrent analyses fit well with this outcome, showing that Y0.1/C/O–CN had a higher photogenerated charge carrier transfer efficiency, which helped to improve the photocatalytic performance.

3.3 Photocatalytic performance

3.3.1 Photocatalytic hydrogen evolution. To determine the efficiency of Y/C/O tridoped g-C_3N_4 photocatalysts, we performed photocatalytic H_2 evolution under visible light irradiation using a co-catalyst of Pt besides TEOA as the electron donor. Fig. 6a compares the H_2 production efficiency of bulk-
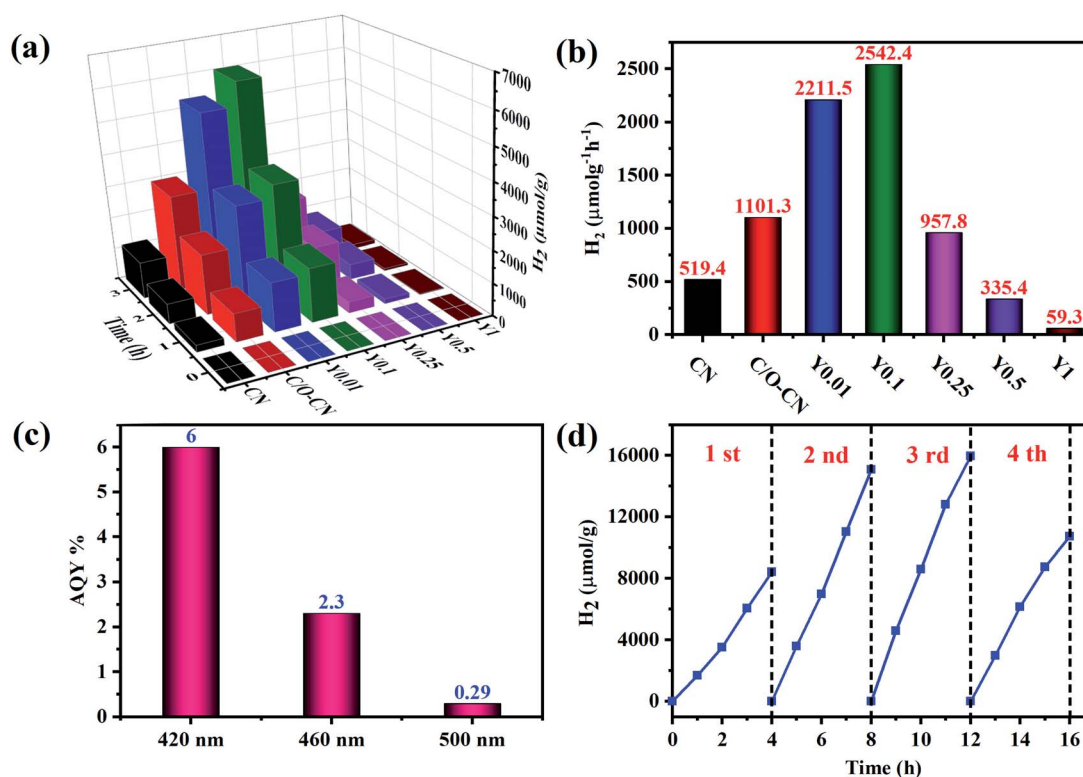

Fig. 6 (a) H_2 evolution performance at λ > 420 nm and (b) photocatalytic H_2 evolution rates over the prepared photocatalysts. (c) Wavelength-dependent AQY and (d) stability test of Y0.1/C/O−CN for H_2 evolution.

CN, C/O–CN, Y0.01/C/O–CN, Y0.1/C/O–CN, Y0.25/C/O–CN, Y0.5/C/O–CN, and Y1/C/O–CN under visible-light irradiation. The highest rate of hydrogen evolution can be achieved at an optimal loading of 5% Pt on the surface of the catalyst (Fig. S5a†). Remarkably, Y0.1/C/O–CN exhibits the most excellent photocatalytic activity under visible-light irradiation, with a rate of H_2 evolution of 2542.4 µmol h^{-1} g^{-1}, which is 2.3 times higher than that of C/O–CN (1101.3 µmol h^{-1} g^{-1}) and ~5 times higher than that of bulk-CN (519.4 µmol h^{-1} g^{-1}). The H_2 production activity of Y/C/O tridoped g-C_3N_4 samples is far superior to that of bulk-CN. The hydrogen generation rate of Yx/C/O–CN reaches the maximum when the Y mass ratio reaches 0.1 g. A further increase in Y mass ratio causes the catalytic properties to deteriorate (Fig. 6b and Table S7†) due to the excess amount of dopant distorting the conduction path and generating new recombination centers for photogenerated charge carriers.[29,40] The above findings indicate that doping, particularly Y, C, and O tri-doping, can significantly improve the catalyst performance through enhancing the active sites and thus increasing the rate of reaction. A comparison of photo-catalytic H_2 production rates between Yx/C/O–CN and other photocatalysts was carried out to illustrate the superiority of this tri-doping system for H_2 generation (see Table S7†). Furthermore, the apparent quantum yield (AQY) calculated for Y0.1/C/O–CN is 6% at 420 nm, 2.3% at 460 nm, and 0.29% at 500 nm, respectively (Fig. 6c). The rapid increase in hydrogen generation and AQY of the Y0.1/C/O–CN can be attributed to its higher surface area that is conducive for hydrogen production and tri-doped C/O/Y atoms that are beneficial for enhancing the electron reduction capability and increasing efficient visible-light harvesting for H_2 evolution.[35,39,41] Moreover, the stability of Y0.1/C/O–CN (Fig. 6d) was investigated under visible-light irradiation and it was stable even after four cycles, indicating superior stability and reusability. Interestingly, as observed from Fig. S5b,† the average HER of Y0.1/C/O–CN increased significantly from 2542.4 µmol h^{-1} g^{-1} at the 1st run to 4595.4 µmol h^{-1} g^{-1} at the end of the 3rd run, but then decreased again at the 4th run. The minor hydrogen production in the first cycle compared to other cycles is due to the time required for the deposition of the Pt co-catalyst on the surface of the Y0.1/C/O–CN photocatalyst,[66] which works as the H_2 generation site. The gradual increase of the H_2 evolution rate can be explained by catalytically active sites being *in situ* formed which requires some time, increasing the reactive surface area and hence the rate of H_2 production in the following cycles.[67,68] Despite these deviations, the consistent photocatalytic performance of the Y0.1/C/O–CN photocatalyst within the four cycles indicates the chemical stability of this photocatalyst.

3.3.2 Photocatalytic activity of dye degradation. A study on the photocatalytic efficiency of all samples under visible-light irradiation was evaluated using dye degradation rates for congo red (CR) and methylene blue (MB) (Fig. 7). Initially, we studied the photocatalytic activity of two model organic dyes (CR and MB) to determine the optimal composition of photo-catalysts capable of exhibiting the highest catalytic activity.

For CR, after 30 min of exposure to light, the Y0.1/C/O–CN catalyst showed the best performance of 98.5% CR degradation compared to the bulk-CN-catalyzed reaction (64.5% dye degradation) (Fig. 7a–c). The performance of the Yx/C/O–CN photocatalyst improved as the mass ratio of Y in the catalyst increased. The maximum performance is achieved when the mass ratio of Y is up to 0.1 g. Further increasing the mass ratio to 1 g leads to deterioration of catalytic properties and decreases CR degradation (86.7%). The photocatalysis reaction of MB dye follows a similar pattern. Here also, Y0.1/C/O–CN demonstrated the highest photocatalytic efficiency among all photocatalysts in this work (Fig. 7d–f). After 110 min of light exposure, bulk CN and C/O–CN-catalyzed reactions showed 33.7 and 48.6% dye degradation, respectively, whereas Y0.1/C/O–CN showed 82.4% degradation in 110 min.

The change of photocatalytic efficiency as a function of photocatalyst composition is illustrated in Fig. S6 and S7 and Table S8.† The UV-vis spectra of CR and MB dyes (Fig. 7a and d) demonstrate the decrease in maximum intensity (λ_{max}) with increasing reaction time for the photodegradation reaction catalyzed by Y0.1/C/O–CN. Fig. 7b and e display the change in the C_t/C_0 ratio for CR and MB dyes over time in the presence of various catalysts (bulk-CN, C/O–CN, Y0.01/C/O–CN, Y0.1/C/O–CN, Y0.25/C/O–CN, and Y0.5/C/O–CN). According to Fig. S8a and b,† the process of photodegradation has pseudo-first-order kinetics. For both CR and MB photocatalytic processes, the pseudo-first-order model provides information about the degradation rates, which are described as follows:

$$\ln\left(\frac{C}{C_0}\right) = -kt$$

where C_0 and C are the initial and final dye concentrations in solution, respectively, t is reaction time, and k is the pseudo-first-order rate constant. The rate constants for the photocatalysts are presented in Fig. 7c and f. It has been noticed that the CN rate constant was 33×10^{-3} and 4×10^{-3} min^{-1} for the CR and MB degradation, respectively. In contrast, the rate constant of Y0.1/C/O–CN is increased to 139×10^{-3} and 17×10^{-3} min^{-1} for photodegradation of both CR and MB, respectively. Table S8† summarizes several commonly used photocatalysts described in the literature for the degradation of CR and MB dyes, with the Y0.1/C/O–CN photocatalyst being the most efficient. Additionally, we performed the Y0.1/C/O–CN-catalyzed photodegradation process using an aqueous solution of CR and MB dyes (25 and 10 ppm, respectively). In 95 minutes, this dye mixture was wholly decomposed by photocatalysis (Fig. S9a and Table S8†).

Y0.1/C/O–CN has conduction and valence band energies of −0.67 and +1.23 eV, respectively. When exposed to visible light, Y0.1/C/O–CN was excited, resulting in photogenerated h^+ in the VB and e^- in the CB. During the photocatalysis process, the photogenerated e^- and h^+ form superoxide and hydroxyl radicals ($O_2^{\cdot-}$ and $^\cdot OH$), which are capable of degrading dye molecules. Additionally, oxidized or reduced compounds are released when the electrons and holes react directly with the dyes. We conducted scavenger tapping studies using *p*-benzoquinone (BQ), isopropanol (IPA), NaCl, and NaNO₃, which act as scavengers for $O_2^{\cdot-}$, $^\cdot OH$, h^+, and e^-, respectively, to understand the function of reactive species better.[69] According to Fig. S9b,†
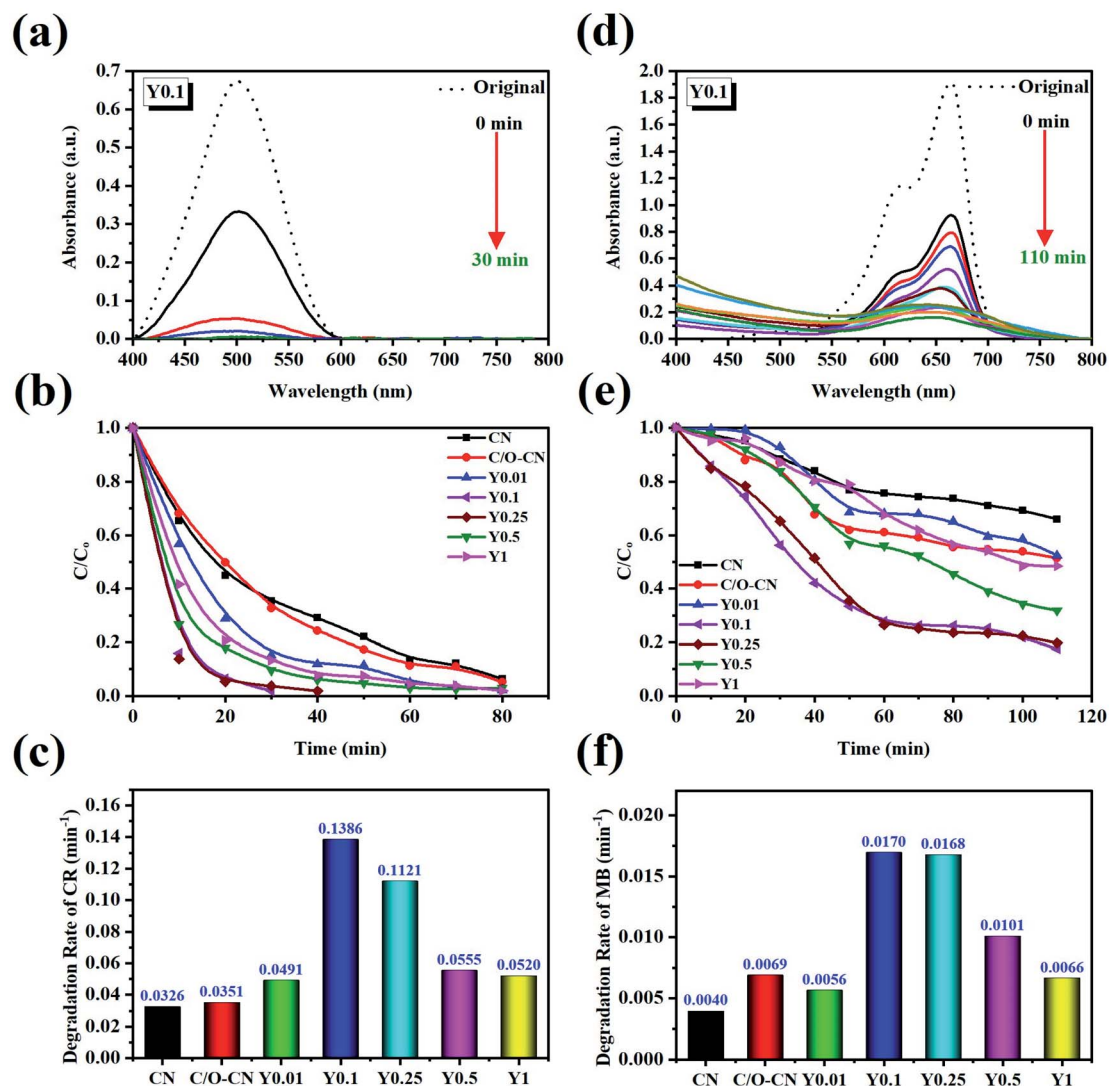
Fig. 7 (a and d) Degradation profiles of CR and MB dyes with the Y0.1/C/O−CN photocatalyst, respectively, (b and e) time-dependent change in CR and MB concentrations, and (c and f) pseudo 1st order rate constants of photocatalytic performances of CR and MB dyes over bulk-CN, C/O−CN, and Y*x*/C/O tridoped CN, respectively.

the CR degradation (98.3%) in the presence of Y0.1/C/O–CN was slightly decreased when IPA, NaCl, and NaNO₃ were added, while it became significantly decreased after adding BQ. The CR degradation efficiencies in the presence of IPA, NaCl, NaNO₃, and BQ were 79.1, 96.2, 71.6, and 25.7%, respectively. The significant decrease in the degradation efficiency for BQ (25.7%) indicates that the primary reactive species responsible for CR dye degradation is the photogenerated $O_2^{\bullet-}$,[70] playing a more significant role than $^{\bullet}OH$, holes, and electrons.

Reusability studies were carried out to gain an understanding of the catalyst's stability. After performing the photocatalysis reaction, the catalyst was washed and dried before being re-used for the following cycle. Fig. S9c† illustrates the recycling study results of the Y0.1/C/O–CN catalyst using CR dye under visible-light irradiation. Our results show that the Y0.1/C/O–CN efficiency decreased by ∼5.5% even after five repeated cycles, indicating that the photocatalyst is relatively stable under reaction conditions.

3.4 DFT calculations

3.4.1 Electronic properties. The purpose of this study is to determine the influence of dopants on the electronic structure of CN. The density of states and band structure of Y/C/O tridoped CN were calculated in comparison to pristine CN. Fig. S10a† and 8a show the optimized crystal structures of CN and Y/C/O tridoped CN. In contrast, the predicted band structure and Brillouin zones are illustrated in Fig. S10c† and 8c. As a result of the DFT calculation, it was determined that the bandgap of pure CN is 1.28 eV, which is consistent with the previously reported results[39,71] and is lower than our experimental value (2.75 eV). The GGA-PBE method is known to underestimate the semiconductor bandgap energy, which leads to a bandgap mismatch. In this case, we are more concerned about the trend of bandgap changes (ΔE_g) after the doping with various atoms, and thus GGA-PBE is used for all computations. As a result of codoping, the bandgap is reduced by around
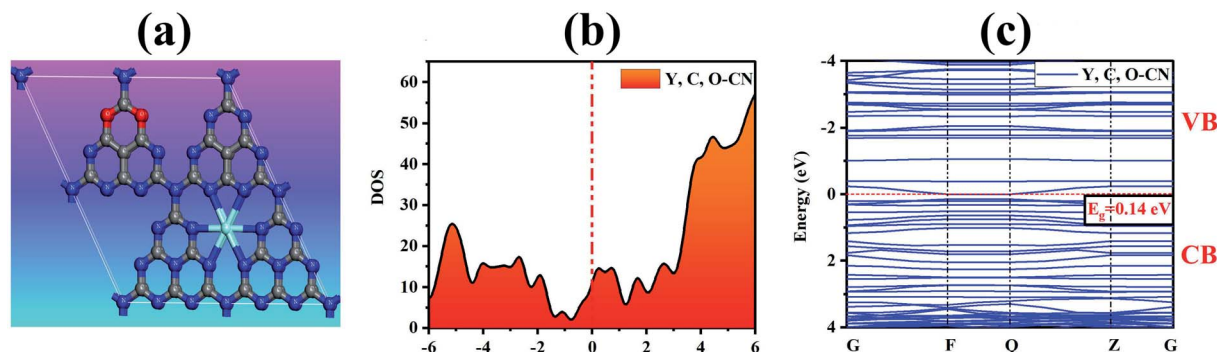
Fig. 8 (a) Optimized $2 \times 2 \times 1$ supercell structure used in the DFT calculations, (b) calculated DOS diagram, and (c) corresponding band structure of Y, C, O tridoped CN, respectively.

1.14 eV, in good agreement with our experimental observations (0.9 eV). The bandgap of the Y/C/O tridoped CN was reduced to 0.14 eV compared to g-C$_3$N$_4$, demonstrating that tridoping with Y, C, and O can reduce the bandgap and result in a significant change in the catalytic properties and improved photocatalysis. As noted in Fig. S10c† and 8c, both pristine CN and Y/C/O tridoped CN are direct-gap semiconductors.[72] Moreover, the Fermi level (E_F) of Y/C/O tridoped CN moved obviously toward a lower energy level. In comparison, the CBM shifted by $\sim$1.14 eV toward a lower energy level (Fig. 8c), indicating that the photocatalyst's redox ability is influenced by the dopants.

The density of states can be used to investigate the electron distribution effect on the catalyst surface (Fig. 8b and S10b†). We estimated the partial density of states (PDOS) and total density of states (TDOS) of pristine and doped CN to gain additional insight into the electronic structure and orbital contribution (see Fig. S10d and e†). The top of the valence band (VBT) in the pristine CN originated from the 2p orbital of N (red lines). In contrast, both C and N 2p orbitals (Fig. S10d†) play an essential role in controlling the conduction band bottom (CBB); it matches previous simulation results.[73] A combination of metal and nonmetal dopants in Y/C/O tridoped CN affects the C 2p and N 2p states in the CB and VB because of interactions between the d, p, and s states of the dopant and the 2p states of C and N atoms. There is an augmentation in the N and C 2p orbitals participating in both CB and VB edges (Fig. S10e†). CB edges are mostly made of 3d orbitals (green lines) of Y and 2p orbitals (red lines) of C, N, and O, respectively, with a minor contribution from 2s orbitals (blue lines) of all atoms (Fig. S10e†). Simultaneously, the VBT is formed by hybridizing the 3d orbital of Y, 2s and 2p orbitals of N, and 2p orbitals of C and O (Fig. S10e†). According to the above results, the impurity levels have the potential to reduce electronic transition energies besides broadening the absorption spectrum.

3.4.2 Optical properties. The optical absorption curves of the pristine CN and Y/C/O tridoped CN are plotted in Fig. S10f.† According to the GGA-PBE method, a significant absorption peak is located at about 350 nm and there is an optical absorption edge (λ_{edge}) near 470 nm for pristine CN, which agrees with the experimental value. These results were in remarkable agreement with the other simulated results near

465 nm.[74] This is mainly attributed to the occurrence of the π–π* transition, suggesting that pure CN is a visible-light photocatalyst. Nevertheless, optical absorption is insufficient in this region, and thus the pristine CN generally exhibits poor photocatalytic performance. After doping, the optical absorption edge moves towards longer wavelength (redshift) by $\sim$92 nm compared to that of CN (Fig. S10f†), indicating that the doped system can significantly expand the visible light response range. It is observed that the Y/C/O tridoped CN absorption curves exhibit a strong absorption tail (Urbach tail) in the UV-visible and infrared regions. According to the optical absorption intensities of CN and Y/C/O tridoped CN, the absorption intensity after doping increases in the UV-visible region with a $\sim$33% increase at 200 nm, consistent with the findings of other simulations,[71] which is assigned to the large dispersion of the CB and impurity level in the bandgap induced by Y, C, and O atoms. The absorption curve area of Y/C/O tridoped CN is larger than that of CN, implying that more electrons of the doped system could be generated upon visible light irradiation. This suggests that the Y, C, and O doping enhances photocatalytic ability. There is likely an electronic transition from the VB to the CB, accounting for the high intensity and broad optical absorption (200–1000 nm).

4. Conclusions

We have successfully synthesized Y/C/O tridoped g-C$_3$N$_4$ photocatalysts by a one-step thermal polymerization method. These photocatalysts display significant absorption in the visible light range, and the bandgap may be controlled by changing the quantity of Y in the photocatalysts, which is necessary for many potential applications. The photocatalytic activity was found to be extremely high for both hydrogen production and pollutant degradation. Among these photocatalysts, Y0.1/C/O tridoped g-C$_3$N$_4$ (optimal doping content) showed the best photodegradation among a variety of model dyes (*e.g.*, CR and MB) in addition to a dye mixture (CR + MB). A photodegradation mechanism was proposed based on the generation of the O$_2^{\bullet-}$ radical during CR dye degradation. The Y0.1/C/O tridoped g-C$_3$N$_4$ shows a significantly improved photocatalytic H$_2$ evolution rate of 2542.4 μmol h^{-1} g^{-1} under visible light (>420 nm),

which is nearly five times greater than that of pure g-C₃N₄, with an AQY of 6% at 420 nm and 0.29% at 500 nm. In this case, the synergistic impact resulting from the unique coexistence of Y, C, and O codoped in g-C₃N₄ with their staggered band structure in the catalysts could explain the observed enhancement. Simultaneously, we determined using DFT that adding Y, C, and O atoms could lower the bandgap, improve visible-light absorption, accelerate charge separation, and improve the photocatalytic properties. As a result, the use of tridoped photocatalysts in the one-pot method represents a novel technique for improving the photocatalytic performance of g-C₃N₄-based photocatalysts.

Conflicts of interest

The authors declare that they have no known competing financial interests or personal relationships that could have appeared to influence the work reported in this paper.

Acknowledgements

References

1 Y. Wang, A. Vogel, M. Sachs, R. S. Sprick, L. Wilbraham, S. J. Moniz, R. Godin, M. A. Zwijnenburg, J. R. Durrant and A. I. Cooper, *Nat. Energy*, 2019, **4**, 746–760.

2 S. Nayak, G. Swain and K. Parida, *ACS Appl. Mater. Interfaces*, 2019, **11**, 20923–20942.

3 S. Nayak and K. Parida, *Sci. Rep.*, 2019, **9**, 1–23.

4 S. Sharma, V. Dutta, P. Raizada, A. A. P. Khan, Q. Van Le, V. K. Thakur, J. K. Biswas, R. Selvasembian and P. Singh, *Environ. Technol. Innovation*, 2021, **24**, 101972.

5 X. Zhang, S. Tong, D. Huang, Z. Liu, B. Shao, Q. Liang, T. Wu, Y. Pan, J. Huang and Y. Liu, *Coord. Chem. Rev.*, 2021, **448**, 214177.

6 C. Wang, C. Yang, J. Qin, S. Rajendran and X. Zhang, *Mater. Chem. Phys.*, 2021, 125299.

7 S. Peiris, H. B. de Silva, K. N. Ranasinghe, S. V. Bandara and I. R. Perera, *J. Chin. Chem. Soc.*, 2021, **68**, 738–769.

8 C. B. Ong, L. Y. Ng and A. W. Mohammad, *Renewable Sustainable Energy Rev.*, 2018, **81**, 536–551.

9 K. Wetchakun, N. Wetchakun and S. Sakulsermsuk, *Ind. Eng. Chem. Res.*, 2019, **71**, 19–49.

10 X. Wang, K. Maeda, X. Chen, K. Takanabe, K. Domen, Y. Hou, X. Fu and M. Antonietti, *J. Am. Chem. Soc.*, 2009, **131**, 1680–1681.

11 W.-J. Ong, L.-L. Tan, Y. H. Ng, S.-T. Yong and S.-P. Chai, *Chem. Rev.*, 2016, **116**, 7159–7329.

12 M. Ismael, *J. Alloys Compd.*, 2020, 156446.

13 C. Prasad, H. Tang, Q. Liu, I. Bahadur, S. Karlapudi and Y. Jiang, *Int. J. Hydrogen Energy*, 2020, **45**, 337–379.

14 M. S. Nasir, G. Yang, I. Ayub, S. Wang, L. Wang, X. Wang, W. Yan, S. Peng and S. Ramakarishna, *Appl. Catal., B*, 2019, **257**, 117855.

15 Q. Hua, X. Zhou, B. Zhang, M. Wang, J. Liu, Y. Wang and L. Jiang, *ACS Sustainable Chem. Eng.*, 2020, **8**, 2919–2930.

16 D. Gogoi, P. Makkar and N. N. Ghosh, *ACS Omega*, 2021, **6**, 4831–4841.

17 J. Liu, Y. Liu, N. Liu, Y. Han, X. Zhang, H. Huang, Y. Lifshitz, S.-T. Lee, J. Zhong and Z. Kang, *Science*, 2015, **347**, 970–974.

18 N. Rahman, J. Yang, M. Sohail, R. Khan, A. Iqbal, C. Maouche, A. A. Khan, M. Husain, S. A. Khattak and S. N. Khan, *Sens. Actuators, A*, 2021, 113128.

19 Y. Gong, M. Li, H. Li and Y. Wang, *Green Chem.*, 2015, **17**, 715–736.

20 M. Ghaemmaghami and R. Mohammadi, *Sustainable Energy Fuels*, 2019, **3**, 2176–2204.

21 Z. Zhao, Y. Sun and F. Dong, *Nanoscale*, 2015, **7**, 15–37.

22 T. O. Ajiboye, A. T. Kuvarega and D. C. Onwudiwe, *Nano-Struct. Nano-Objects*, 2020, **24**, 100577.

23 J. Zou, Y. Yu, W. Yan, J. Meng, S. Zhang and J. Wang, *J. Mater. Sci.*, 2019, **54**, 6867–6881.

24 Z. Shu, Y. Wang, W. Wang, J. Zhou, T. Li, X. Liu, Y. Tan and Z. Zhao, *Int. J. Hydrogen Energy*, 2019, **44**, 748–756.

25 P. Deng, J. Xiong, S. Lei, W. Wang, X. Ou, Y. Xu, Y. Xiao and B. Cheng, *J. Mater. Chem. A*, 2019, **7**, 22385–22397.

26 V. Balakumar, H. Kim, J. W. Ryu, R. Manivannan and Y.-A. Son, *J. Mater. Sci. Technol.*, 2020, **40**, 176–184.

27 G. Zhang, Z.-A. Lan, L. Lin, S. Lin and X. Wang, *Chem. Sci.*, 2016, **7**, 3062–3066.

28 P. Niu, G. Liu and H.-M. Cheng, *J. Phys. Chem. C*, 2012, **116**, 11013–11018.

29 J. Zhang, X. Chen, K. Takanabe, K. Maeda, K. Domen, J. D. Epping, X. Fu, M. Antonietti and X. Wang, *Angew. Chem., Int. Ed.*, 2010, **49**, 441–444.

30 J. Meng, X. Wang, Y. Liu, M. Ren, X. Zhang, X. Ding, Y. Guo and Y. Yang, *Chem. Eng. J.*, 2021, **403**, 126354.

31 Y. Wang, H. Wang, F. Chen, F. Cao, X. Zhao, S. Meng and Y. Cui, *Appl. Catal., B*, 2017, **206**, 417–425.

32 K. Chen, Z. Chai, C. Li, L. Shi, M. Liu, Q. Xie, Y. Zhang, D. Xu, A. Manivannan and Z. Liu, *ACS Nano*, 2016, **10**, 3665–3673.

33 S. Khan, H. Ikari, N. Suzuki, K. Nakata, C. Terashima, A. Fujishima, K.-i. Katsumata and V. Rodríguez-González, *ACS Omega*, 2020, **5**, 23081–23089.

34 G. Yang, H. Lei, H. Tao, X. Zheng, J. Ma, Q. Liu, W. Ke, Z. Chen, L. Xiong and P. Qin, *Small*, 2017, **13**, 1601769.

35 Y. Wang, Y. Li, X. Bai, Q. Cai, C. Liu, Y. Zuo, S. Kang and L. Cui, *Catal. Commun.*, 2016, **84**, 179–182.

36 Y. Ding, Y. Tang, L. Yang, Y. Zeng, J. Yuan, T. Liu, S. Zhang, C. Liu and S. Luo, *J. Mater. Chem. A*, 2016, **4**, 14307–14315.

37 J. Fu, B. Zhu, C. Jiang, B. Cheng, W. You and J. Yu, *Small*, 2017, **13**, 1603938.

38 P. Qiu, C. Xu, H. Chen, F. Jiang, X. Wang, R. Lu and X. Zhang, *Appl. Catal., B*, 2017, **206**, 319–327.

39 L. Jing, D. Wang, M. He, Y. Xu, M. Xie, Y. Song, H. Xu and H. Li, *J. Hazard. Mater.*, 2021, **401**, 123309.

40 J. Wu, N. Li, X.-H. Zhang, H.-B. Fang, Y.-Z. Zheng and X. Tao, *Appl. Catal., B*, 2018, **226**, 61–70.

41 X. Zheng, Q. Zhang, T. Chen, Y. Wu, J. Hao, C. Tan, P. Chen, F. Wang, H. Liu and W. Lv, *J. Hazard. Mater.*, 2020, **386**, 121961.

42 H. Wang, B. Wang, Y. Bian and L. Dai, *ACS Appl. Mater. Interfaces*, 2017, **9**, 21730–21737.

43 H. Ma, Y. Li, S. Li and N. J. A. S. S. Liu, *Appl. Surf. Sci.*, 2015, **357**, 131–138.

44 H. Ma, S. Zhao, S. Li and N. Liu, *RSC Adv.*, 2015, **5**, 79585–79592.

45 S. J. Clark, M. D. Segall, C. J. Pickard, P. J. Hasnip, M. I. Probert, K. Refson and M. C. Payne, *Z. Kristallogr. - Cryst. Mater.*, 2005, **220**, 567–570.

46 J. P. Perdew, K. Burke and M. Ernzerhof, *Phys. Rev. Lett.*, 1996, **77**, 3865.

47 J. P. Perdew, M. Ernzerhof and K. Burke, *J. Chem. Phys.*, 1996, **105**, 9982–9985.

48 S. Zhao, Y. Zhang, Y. Wang, Y. Zhou, K. Qiu, C. Zhang, J. Fang and X. Sheng, *J. Power Sources*, 2017, **370**, 106–113.

49 Y. Wang, F. Silveri, M. K. Bayazit, Q. Ruan, Y. Li, J. Xie, C. R. A. Catlow and J. Tang, *Adv. Energy Mater.*, 2018, **8**, 1801084.

50 L. Kong, Y. Ji, Z. Dang, J. Yan, P. Li, Y. Li and S. Liu, *Adv. Funct. Mater.*, 2018, **28**, 1800668.

51 L. Wang, Y. Hou, S. Xiao, F. Bi, L. Zhao, Y. Li, X. Zhang, G. Gai and X. Dong, *RSC Adv.*, 2019, **9**, 39304–39314.

52 Z. Tong, D. Yang, T. Xiao, Y. Tian and Z. Jiang, *Chem. Eng. J.*, 2015, **260**, 117–125.

53 X. Peng, J. Li, X. Liu, L. Yi, P. Cai and Z. Wen, *Int. J. Hydrogen Energy*, 2021, **46**, 28591–28601.

54 J. Qin, S. Wang, H. Ren, Y. Hou and X. Wang, *Appl. Catal., B*, 2015, **179**, 1–8.

55 S. Hu, L. Yang, Y. Tian, X. Wei, J. Ding, J. Zhong and P. Chu, *Appl. Catal., B*, 2015, **163**, 611–622.

56 X. Gao, B. Zhou and R. Yuan, *Environ. Eng. Res.*, 2015, **20**, 329–335.

57 J. K. Rajput, *J. Electroanal. Chem.*, 2020, **878**, 114605.

58 B. Su, H. Huang, Z. Ding, M. B. Roeffaers, S. Wang and J. Long, *J. Mater. Sci. Technol.*, 2022, **124**, 164–170.

59 B. Li, F. Wei, B. Su, Z. Guo, Z. Ding, M.-Q. Yang and S. Wang, *Mater. Today Energy*, 2022, 100943.

60 B. Li, W. Wang, J. Zhao, Z. Wang, B. Su, Y. Hou, Z. Ding, W.-J. Ong and S. Wang, *J. Mater. Chem. A*, 2021, **9**, 10270–10276.

61 X. Lin, Z. Xie, B. Su, M. Zheng, W. Dai, Y. Hou, Z. Ding, W. Lin, Y. Fang and S. Wang, *Nanoscale*, 2021, **13**, 18070–18076.

62 R. Wang, P. Yang, S. Wang and X. Wang, *J. Catal.*, 2021, **402**, 166–176.

63 A. B. Jorge, D. J. Martin, M. T. Dhanoa, A. S. Rahman, N. Makwana, J. Tang, A. Sella, F. Corà, S. Firth and J. A. Darr, *J. Phys. Chem. C*, 2013, **117**, 7178–7185.

64 Y. Zhou, L. Zhang, W. Huang, Q. Kong, X. Fan, M. Wang and J. Shi, *Carbon*, 2016, **99**, 111–117.

65 X. Zhang, X. Xie, H. Wang, J. Zhang, B. Pan and Y. Xie, *J. Am. Chem. Soc.*, 2013, **135**, 18–21.

66 P. Edalati, X.-F. Shen, M. Watanabe, T. Ishihara, M. Arita, M. Fuji and K. Edalati, *J. Mater. Chem. A*, 2021, **9**, 15076–15086.

67 W. Zhou, T. Jia, D. Zhang, Z. Zheng, W. Hong and X. Chen, *Appl. Catal., B*, 2019, **259**, 118067.

68 W.-C. Lin, W.-D. Yang, I.-L. Huang, T.-S. Wu and Z.-J. Chung, *Energy Fuels*, 2009, **23**, 2192–2196.

69 S. Ghattavi and A. Nezamzadeh-Ejhieh, *Composites, Part B*, 2020, **183**, 107712.

70 J. Wang, G. Wang, B. Cheng, J. Yu and J. Fan, *Chin. J. Catal.*, 2021, **42**, 56–68.

71 D. K. Gorai and T. Kundu, *J. Manuf. Process.*, 2020, **35**, 625–634.

72 X. She, L. Liu, H. Ji, Z. Mo, Y. Li, L. Huang, D. Du, H. Xu and H. Li, *Appl. Catal., B*, 2016, **187**, 144–153.

73 J. Cui, S. Liang, X. Wang and J. Zhang, *Mater. Chem. Phys.*, 2015, **161**, 194–200.

74 S. Lu, C. Li, H. Li, Y. Zhao, Y. Gong, L. Niu, X. Liu and T. Wang, *Appl. Surf. Sci.*, 2017, **392**, 966–974.